THE JOURNAL OF PHYSICAL CHEMISTRY C

pubs.acs.org/JPCC Article

Peculiar Magnetic and Transport Properties of $CuFeS_2$: Defects Play a Key Role

Jiřá Navrátil, Petr Levinský, Jiří Hejtmánek, Mariia Pashchenko, Karel Knížek, Lenka Kubíčková, Tomáš Kmječ, and Čestmír Drašar*

Cite This: https://dx.doi.org/10.1021/acs.jpcc.0c06490 Read Online

ACCESS | Metrics & More | Article Recommendations | Supporting Information

ABSTRACT: Our study targets some of the long-standing questions concerning the somewhat mysterious properties of chalcopyrite $CuFeS_2$. We show that defect chemistry in connection with charge transfer within the structure is responsible for the unusual electronic and magnetic properties of $CuFeS_2$. Specifically, our model addresses weak ferromagnetism and the high mobility of carriers on the background of a rigid antiferromagnetic structure. We show that defect structure can, counterintuitively, boost the mobility of free carriers due to defect-modified charge transfer. Further, the defect-modified charge transfer induces the weak ferromagnetism both in the Cu- and Fe-sublattice. This new view opens up space for further investigations and applications of charge transfer compounds.

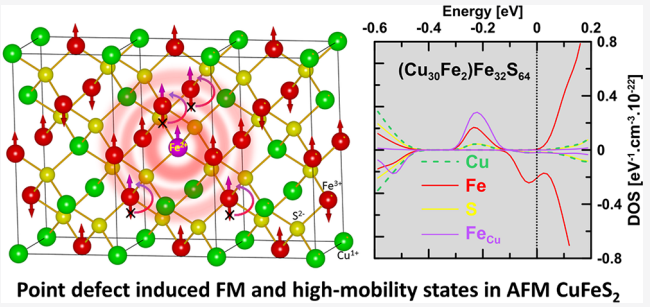

Point defect induced FM and high-mobility states in AFM $CuFeS_2$

1. INTRODUCTION

Chalcopyrite, $CuFeS_2$, has been recognized as the world's most important and most abundant copper ore for a thousand years. Its unique electrical, magnetic, thermal, and optical properties have already attracted attention from scientists since the dawn of the semiconductor era.[1−9] Owing to these properties, $CuFeS_2$ has been widely studied for its potential utilization in photovoltaics,[10] spintronics,[11] and thermoelectrics.[12−16]

$CuFeS_2$, crystallizing in a tetragonal structure with space group $I\bar{4}2d$,[17] is an antiferromagnetic (AFM) semiconductor with a comparatively high Neel temperature (T_N = 823 K[5]) that can be understood in terms of very low anion-cation charge-transfer energy facilitating the AFM order.[18,19] For the complexity of its nature, $CuFeS_2$ has been the subject of theoretical and experimental investigations for more than a century.[20] Nevertheless, experimental investigations have been hindered by its tendency to undergo decomposition or a phase transition leading to the formation of extraneous phases.[21,22] One of the most striking points for this material is the number of unpaired electrons of iron and its ground state in relation to the magnetic and spectroscopic properties.[18,19,23] Nevertheless, there are many points that have yet to be explained. Namely, Mössbauer spectroscopy shows the undoubted presence of trivalent high-spin iron in the chalcopyrite structure,[24] indicating five unpaired electrons in the d orbitals of Fe. In contrast, a considerably lower magnetic moment is reported based on neutron diffraction,[4,22] X-ray emission spectroscopy,[19,23] and theoretical calculations.[25−28] However, most of the calculations combined with spectroscopy techniques neglect Fe d-band dispersion and treat the Fe ions as impurities within an anion-hosting band structure.[18,19,23]

The exact valence state of copper ions remains in debate, although it is clear that number of d electrons is slightly lower than 10, which would correspond to the Cu^{+1} state.[22,29,30] The electrical transport complexity is documented by a rather wide range of reported band-gap values derived from various experiments (i.e., 0.33 eV,[31] 0.53 eV,[3] and 2.6 eV[5]). Furthermore, the electron mobility spans a rather wide range from 10^{-3} to 10^{2} $cm^2\ V^{-1}\ s^{-1}$ depending on the temperature and doping and Fermi level (E_F). Thus, the nature of the electrical transport can be described within various models starting with hopping transport in the low-temperature region and, inevitably, ending with band transport at higher temperatures. Some peculiar interactions have been included to account for the "mysterious behaviour"[23] of chalcopyrite including negative charge transfer (CT) energy. The contribution of CT-driven hybridization between the Fe3d and S3p orbitals has also been discussed previously.[19] Furthermore, band calculations can shed more light on the delocalized Fe3d electrons,[26,32,33] thus attributing markedly to a consistent picture as for the spectroscopic properties and AFM ordering. However, the magnitude of the free-carrier

Received: July 16, 2020
Revised: August 25, 2020
Published: August 27, 2020

mobility (≈100 $cm^2\ V^{-1}\ s^{-1}$) observed in the present paper and ref 34 is in contrast with the electron mobility within the AFM order of $CuFeS_2$. Thus, we miss a clue for the true mechanism of charge transport in pristine and doped chalcopyrite, although the spectroscopic and magnetic properties may be addressed properly.

In addition, over the past decade, $CuFeS_2$ has been the subject of extensive research as for its potential in thermoelectric applications.[13,15,35−38] Most studies have focused on the optimization of the properties of $CuFeS_2$ by a proper doping, and only mid-temperature properties (above 300 K) for the materials have been investigated. Similarly, we published a study of the partial replacement of Cu atoms by Pd in the $Cu_{1-x}Pd_xFeS_2$ system in the mid-temperature region.[39] In the present paper, we employ a wide set of low-temperature measurements, intending to obtain a coherent picture of all the material properties. Thus, based on low-temperature transport and magnetic measurements for a series of $Cu_{1-x}Pd_xFeS_2$ samples, we attempt to draw a picture that can be generally applied for the hosting compound $CuFeS_2$. To make the discussion more conclusive, we include some other nonstoichiometric compositions with the aim to manipulate the concentration of native defects, which play, in our view, a crucial role in $CuFeS_2$. Thus, the present paper differs substantially from previous papers as it recognizes point defects as an important ingredient of the nature of $CuFeS_2$.[34]

We consider two profoundly different groups of native (intrinsic) defects inherent to the $CuFeS_2$ structure. The first group consists of intrinsic point defects (IPDs) such as antisites and vacancies that are invariable as for time and place in a sample under exploration. The second group appears as a result of anion-cation charge transfer (CT) and is called "seeded CT defects". Both groups can be understood as defect levels. The latter, however, is considered to participate in extended states that are seeded by IPDs. We argue that this accounts for the surprisingly high mobility of free carriers and the small magnetic moment observed on Cu.[22,29]

First, we argue that, for the case of perfectly crystalline stoichiometric $CuFeS_2$, any "disorder" stems only from charge fluctuation on the Fe site due to charge transfer from sulfur to iron.[19,23] The CT fluctuations can facilitate hopping of electrons from site to site at low temperatures. We start with the conclusions by Sato et al.[23] who argue that the CT energy Δ is close to zero and perhaps even negative in contrast to the d-d spin fluctuation energy U (≈4 eV). This results in a ground state composed of Fe^{+1}, Fe^{+2}, and Fe^{+3} states; generally, Fe^{+3-x} states. Despite the CT fluctuations from sulfur to iron sites, the structure maintains the AFM order. In fact, CT boosts the AFM order. We suggest, however, that Fe ions can also be coupled ferromagnetically in the presence of IPDs, which serve as FM centers, i.e., $-Fe^{+3}-S^{-2}-Fe^{+3}-S^{-2}-Fe^{+3}-$ AFM superexchange bridge is replaced by FM superexchange bridge, e.g., $-Fe^{+3-x}-S^{-1}-Fe^{+3-x}-S^{-2}-Fe^{+3-x}-$. Thus, the CT is the driving force for the robust AFM order present in defect-free $CuFeS_2$ but induces a weak FM coupling when seeded by IPDs. Although the Fe ions in antiferromagnetic $CuFeS_2$ are often analyzed as an "impurity" in an anion continuum or within a cluster approach,[18,23] the Fe and Cu atoms naturally form a band with Bloch-like transport and a rather high mobility in the case of the FM order.

Second, we argue that, for the case of perfectly crystalline stoichiometric $CuFeS_2$, the Cu atoms carry no magnetic moment and are excluded from free-carrier transport. Namely, Cu-based bands are far from the Fermi level and adopt a formally $3d^{10}$ configuration.[33] However, IPDs may induce a net magnetic moment on the Cu site, resulting in a $3d^{10-x}$ configuration, which facilitates band transport within the Cu d bands. In other words, due to defect-induced FM-like delocalization, electrons can move within such a band with much higher mobility than they would do within a strictly localized Fe-based AFM structure. Additionally, this explains the magnetic moment observed on Cu sites using neutron diffraction.[22,40] We note that the sulfur−iron CT fluctuation may also induce a small magnetic moment on Cu at higher temperatures.[33] We have found extrinsic doping to be mostly ineffective irrespective of the sublattice being substituted (e.g., Co, Cr, Mn, P, and Cl). Thus, we assume that delocalized electrons stem mainly from IPDs, even in extrinsically doped samples (except for low concentrations of Pd). The concentration of electrons can, however, be increased by doping through a shift in stoichiometry induced by dopants, as in the present case for Pd. The most prominent intrinsic defect is antisite (AS) defect Fe_{Cu}, which is accessible in comparatively high concentrations via a shift in the Cu/Fe stoichiometry by Zn or Pd doping.[37,39] Furthermore, we assume a rather low concentration of sulfur vacancies V_S. As we show below, both Fe_{Cu} and V_S, result, in fact, in Fe^{+2} sites with both donor (acceptor) and FM seeding ability. Although the structure of $CuFeS_2$ remains AFM as a whole, the defects can induce an FM nature locally in terms of energy and wave vector space.[26] The results from DFT calculations are found to be coherent with the conclusions drawn from the transport and magnetic measurements. Although every single method provides just a part of the picture, one obtains a rather complete picture when taken as a whole.

2. EXPERIMENTAL SECTION

A series of polycrystalline samples with the nominal composition $Cu_{1-x}Pd_xFeS_2$ (x = 0, 0.005, 0.01, 0.02, 0.1) was synthesized from a mixture of pure elements obtained from Sigma-Aldrich including Cu (4N shots), Pd (4N powder), Fe (4N granular), and S (5N powder). Moreover, samples with the composition $Cu_{1.02}Fe_{0.98}S_2$ and $Cu_{1-x}Fe_xS_2$ (x = 0.01, 0.02) were prepared for comparison. All details on the sample synthesis were given in our previous work on the $Cu_{1-x}Pd_xFeS_2$ system[39] where also structural and compositional analysis can be found in detail.

Electrical resistivity, Seebeck coefficient, and thermal conductivity of the samples between 2 and 310 K were measured simultaneously employing the four-probe method. Thin silver wire leads were affixed to the bar-shaped samples of typical dimensions 1 × 2 × 12 mm^3 with nickel paste. The $Cu_{1-x}Pd_xFeS_2$ samples were measured using the thermal transport option (TTO) of the Quantum Design PPMS instrument. Due to its high resistivity, the $Cu_{1.02}Fe_{0.98}S_2$ sample was measured using a homemade setup and the data points above 10^4 Ω·m (several MΩ) should be regarded as indicative only. Hall effect was measured using the electrical transport option (ETO) of the PPMS instrument between −2 and 2 T on bar-shaped samples with four silver leads welded to the sample.

The magnetic properties were investigated by the SQUID magnetometer Quantum Design MPMS-XL7 with the reciprocating sample option. Measurements were performed on small samples (sized about 1 × 1 × 1 mm^3 and weighing about 10 mg) placed in between two concentric transparent

https://dx.doi.org/10.1021/acs.jpcc.0c06490
J. Phys. Chem. C XXXX, XXX, XXX−XXX

plastic straws without the use of any glue. The samples were reciprocated between the pick-up coils at 1 Hz with an amplitude of 4 cm. Isothermal magnetization curves $M(H)$ were obtained between by stepping the field in driven mode between 7, −7, and 7 T. When changing the sample temperature, the field was zero. For thermoremanence measurements, the samples were magnetized to 7 T at 3 K, the field was then reduced to 0 and the magnet quenched. Subsequently, the evolution of the remanent magnetization was measured while sweeping the temperature from 3 to 390 K at a rate of 2 K/min below 9 K and 5 K/min above 9 K.

The transmission ^{57}Fe Mössbauer spectroscopy of $CuFeS_2$ and $Cu_{0.9}Pd_{0.1}FeS_2$ powder samples was employed to study the local magnetic properties of the samples (see Supporting Information, section C). The spectra were acquired at 4.2 K and room temperature by using the ^{57}Co/Rh source and evaluated in the Confit[41] and Recoil[42] programs, and the calibration of velocities and isomer shifts was performed with respect to an α-Fe foil at room temperature. The in-field spectra at 6 T were measured at 4.2 K in a liquid-helium bath cryostat by Janis Research with the orientation of the applied field perpendicular to the direction of γ-rays.

The calculations were made with the WIEN2k program.[43] This program is based on the density functional theory (DFT) and uses the full-potential linearized augmented plane-wave (FP LAPW) method with the dual basis set. The space of the unit cell is divided into atomic spheres and the interstitial region. The calculations were made either in the basic unit cell with formula units $Z = 4$ and for the defect simulations in the eight times enlarged supercell with $Z = 32$ defined by aS = 2a, bS = 2b, and cS = 2c. The number of k-points in the irreducible part of the Brillouin zone was 108 for the basic unit cell (Z = 4) and 93 for the supercell ($Z = 32$). All calculations were spin-polarized. For the exchange correlation potential, we adopted the generalized gradient approximation (GGA) form.[44] To improve the description of 3d electrons, we used the GGA+U method. In this method, an orbitally dependent potential is introduced for the chosen set of electron states, i.e., for the 3d states. This additional potential has an atomic Hartree−Fock form but with screened Coulomb and exchange interaction parameters. The fully localized limit version of the GGA+U method was employed. The parameters $U = 2$ eV and $J = 1$ eV were used. Several parameters of U and J were tested in the GGA+U calculations resulting in different sizes of band gap. The presented results were obtained with parameters $U = 2$ eV and $J = 1$ eV, which were selected according to the best agreement of the calculated and the experimentally determined band gap.[3,31] The calculations of the electrical transport properties were done within Boltzmann transport theory using the BoltzTrap package[45] under the constant relaxation time approximation for the charge carriers.

3. RESULTS AND DISCUSSION

3.1. Charge Transport Properties. The low-temperature resistivity showing typical semiconducting behavior is depicted in Figure 1. It can be concluded that Pd substitution for Cu, i.e., point defect Pd_{Cu}, leads to a substantial decrease in the resistivity, which generally indicates the donor effect of the Pd. The equation $xPd^{+2}S + Cu^{+1}FeS_2 \rightarrow Cu_{1}^{+1}Pd_{x}^{+2}FeS_{2+x}$ reflects the formation of Pd_{Cu}^{+2} point defects that can donate electrons through excitation $Pd_{Cu}^{+2} \rightarrow Pd_{Cu}^{+3} + e^-$. Pd_{Cu}^{+3} is available in tetrahedral coordination due to the $(e_g)^4(t_{2g})^3$ configuration. However, the doping effect is largely connected with the shift

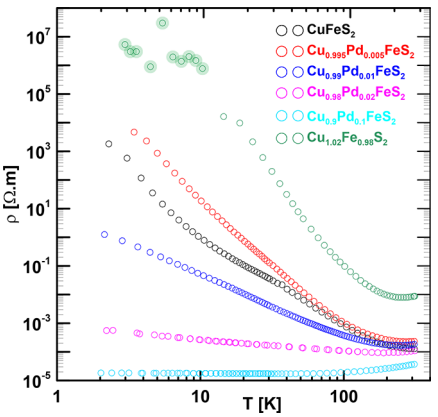

Figure 1. Temperature-dependent electrical resistivity of $Cu_{1-x}Pd_xFeS_2$ ($0 \geq x \geq 0.1$) and $Cu_{1.02}Fe_{0.98}S_2$. Green shaded symbols above 10^4 Ω·m (≈10 MΩ) are at the facility resolution limit and should be considered as a tendency.

in the Cu/Fe stoichiometry. Thus, for $x > 0.01$, the equation $(Cu_{1-x}^{+1}Pd_x^{+2})FeS_2 \rightarrow (Cu_{1-x}^{+1}Pd_{x-y}^{+2}Fe_y^{+2})FeS_2 + yPdS$ reflects the donor effect leading to the degenerate state for $x = 0.1$.[39] Namely, the excitation $Fe_{Cu}^{+2} \rightarrow Fe_{Cu}^{+3} + e^-$ represents the doping process. The excess of Pd is segregated during the growth in the form of PdS.[39] We performed a detailed exploration of the resistivity data using $\ln \rho = f(T^{-1/p})$ fitting with the aim of revealing the nature of charge transport in detail (see Supporting Information, section A). The examined temperature range is split into three regions with different y values, indicating three different charge transport mechanisms in accordance with the analysis given in refs 34, 46. Generally, the high-temperature region can be fitted using an Arrhenius plot $\ln \rho = f(T^{-1})$ with a rather low activation energy $E = 25$ meV connected with band transport. The mid-region is dominated by 3D Mott variable-range hopping (VRH),[47] while Efros−Shklovskii VRH dominates in the low-temperature region, especially for samples with a very low concentration of free carriers. A very low free-carrier concentration in $Cu_{1.02}Fe_{0.98}S_2$ guarantees an Efros−Shklovskii VRH mechanism up to ∼100 K, while no Efros-Shklovskii VRH mechanism is observed in heavily doped samples due to the rather high concentration of electrons. Figure 2 depicts the Hall coefficient R_H as a function

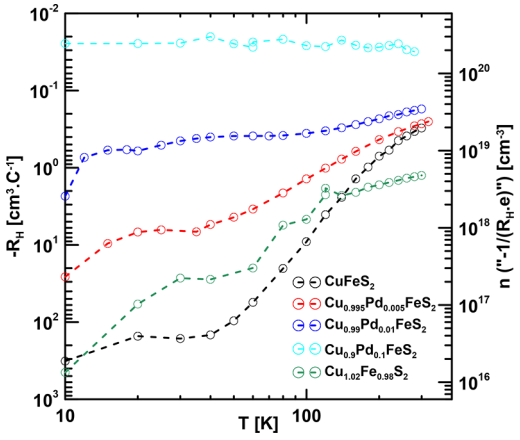

Figure 2. Hall coefficient R_H and calculated Hall free-carrier concentration n $(-1/(R_H \cdot e))$ as a function of temperature for $Cu_{1-x}Pd_xFeS_2$ ($0 \geq x \geq 0.1$) and $Cu_{1.02}Fe_{0.98}S_2$ samples.

https://dx.doi.org/10.1021/acs.jpcc.0c06490
J. Phys. Chem. C XXXX, XXX, XXX−XXX

of temperature and corresponding Hall free-carrier concentration n_H obtained from the relation $n_H = -1/(R_H \cdot e)$, where e is the electron charge. For non-degenerate samples, we observe a common feature: a very small concentration of electrons is generated below 10 K and saturation between 10 and 40 K, thus producing a shallow minimum. However, we note that such a minimum in R_H is attributable to thermal hopping as well (see, e.g., Avdonin[48]). Then, due to another excitation, the free-carrier concentration steeply grows from 40 to 50 K up to 300 K. This excitation can be attributed to AS defects Fe_{Cu}[37,39] for $Cu_{1-x}Pd_xFeS_2$ and sulfur vacancies for $Cu_{1.02}Fe_{0.98}S_2$. This excitation disappears when approaching the degenerate regime, and the highly degenerated $Cu_{0.9}Pd_{0.1}FeS_2$ sample shows a high and almost constant free-carrier concentration ($\sim 2.10^{20}$ cm^{-3}) in the whole measured temperature range. This indicates a merging of the defect level (band) into the conduction band minimum with increasing concentration of AS defects, which is in accordance with DFT calculations, as described below. In contrast to the stoichiometric sample, the free-carrier concentration in the $Cu_{1.02}Fe_{0.98}S_2$ sample remains to be very low at 300 K (4.5×10^{18} cm^{-3}). We premise that magnetic measurements insinuate a small concentration of sulfur vacancies and depletion of AS defects Fe_{Cu}, which is consistent with the overstoichiometry of copper. Some remarks should be pointed out here. First, the resistivity of the $Cu_{1.02}Fe_{0.98}S_2$ sample is so high that, at low temperatures, the accuracy of the data is at the limit for the used equipment and may somewhat deviate from true values. More importantly, the hopping mechanism may become dominant for non-degenerate samples at very low temperatures (see Supporting Information, section A). Thus, utilization of a simple formula for the Hall concentration is inaccurate under such circumstances.[48] Therefore, we consider that such analysis of the Hall data is reliable for all degenerate samples, but for non-degenerate samples, it is reliable only above ≈80 K. Similarly, this applies to the calculated Hall mobility μ_H (Figure 3), and we consider

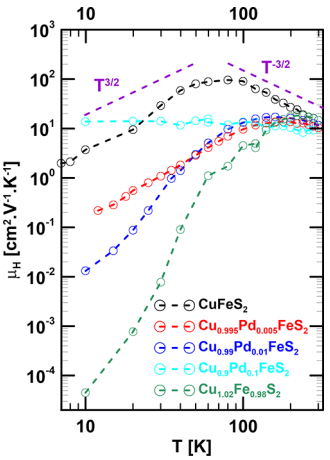

Figure 3. Hall mobility μ_H (R_H/ρ) as a function of temperature for $Cu_{1-x}Pd_xFeS_2$ ($0 \geq x \geq 0.1$) and $Cu_{1.02}Fe_{0.98}S_2$ samples.

the low-temperature data for the non-degenerate samples on a relative scale only. Strikingly, the magnitude of the mobility (and resistivity) above 80 K contradicts the antiferromagnetic (AFM) order of the hosting structure for stoichiometric $CuFeS_2$ and Pd-doped samples. Namely, a strict AFM order dictates localization of d electrons. However, we observe electric transport within a dispersive band. We address this issue in the following section.

3.2. Intrinsic Defects and Band-Structure Calculations. The band structure proposed from optical measurements for $CuFeS_2$ single crystals hints at the existence of "an upper valence band" or "an additional conduction band", i.e., a band lying inside the broader energy gap of ≈0.5 eV. This band is mostly formed by the hybridized 3d orbitals of Fe and 3p orbitals of S, and its edge corresponds to the initial point of the band-to-band transition.[7,26,33] The present results obtained from DFT calculations for the defect-free structure are in accordance with previously published data.[33,49]

In our previous paper,[39] we assumed a specific shape for the bottom of the conduction band to account for evidence of high-mobility Fe d orbital-derived electrons. However, based on the present experiments and DFT calculations, we revise the picture drawn in our previous paper. In our view, the appearance of both "light and heavy" electrons is connected with a non-negligible concentration of IPDs. The experimental and theoretical data available point toward the presence of two types of intrinsic defects, Fe_{Cu} and V_S. This explains the "specific shape of the conduction band edge" mentioned in our previous paper. Namely, the occurrence of V_S and Fe_{Cu} (or their combination) results in distinct FM states close to the Fermi level (Figure 4AA,B). This conclusion is in accordance with free-carrier concentration-dependent FM, as discussed for the magnetic properties (Section 3.3). Thus, we assume two types of free carriers and two types of corresponding magnetic order exist in $CuFeS_2$, with both connected to IPDs.

The starting point of our consideration is the neutrality of $CuFeS_2$ as a whole. An Fe atom placed on the Cu site can adopt, e.g., Fe_{Cu}^{+3}, Fe_{Cu}^{+2}, or Fe_{Cu}^{+1} states. This, in turn, induces Fe_{Fe}^{+1}, Fe_{Fe}^{+2}, or Fe_{Fe}^{+3} states, respectively, for neighboring Fe sites within Fe_2Cu_2S tetrahedra. This may be reflected in FM coupling within $-Fe^{+3-z}-S^{-2}-Fe^{+3-z}-S^{-2}-Fe^{+3-z}-$ bridges, i.e., the formation of seeded CT defects (Figure 5(left)). The AS defect can be viewed as a hard excitation. Similarly, Fe_{Cu} may dictate the CT nature within $-Cu^{+1-z}-S^{-2}-Cu^{+1-z}-S^{-2}-Cu^{+1-z}-$ bridges that induces a weak FM (Figure 5(right)). The sulfur vacancy V_S plays a similar role. Accepting the ionic picture of $CuFeS_2$ in the form of $Cu^{+1}Fe^{+3}S_2^{-2}$,[5,6,17,23] we have to recognize that V_S, in fact, represents two Fe^{+2} point defects. Namely, the corresponding Fe d electrons remain localized at Fe atoms instead of being transferred to sulfur within the ionic−covalent bond. Thus, a missing sulfur atom produces a $-Fe^{+2}-V_S-Fe^{+2}-$ defect. Strictly speaking, from a purely ionic view, each Fe transfers 0.75 electrons to S in Fe_2Cu_2S tetrahedra. Thus, the defect should read $-Fe^{+2.25}-V_S-Fe^{+2.25}-$. We adhere to the former simplified notation since it makes no difference in our qualitative discussion. The formation of such a defect, in turn, implies the appearance of, e.g., $-Fe^{+2}-S-Fe^{+3}-$ chains in the neighborhood, which induces FM coupling instead of the common AFM coupling in the hosting structure[50,51] (Figure 6). Moreover, the sulfur atom is coordinated by two Fe atoms and two Cu atoms (Fe_2Cu_2S tetrahedra). The Cu atoms also keep their electrons when neighboring with V_S, which formally reads as $-Cu^{+0.75}-V_S-Cu^{+0.75}-$. Thus, similar to Fe_{Cu}, V_S may induce a weak FM coupling within $-Cu^{+1-z}-S^{-2}-Cu^{+1-z}-S^{-2}-Cu^{+1-z}-$ seeded CT defects. In this case, the formal charge of copper is lower than +1, resulting, formally, in a $3d^{10-x}$ configuration for a single ion. Note that, in defect-free $CuFeS_2$, indirect participation of Cu atoms in CT is also likely to induce a

https://dx.doi.org/10.1021/acs.jpcc.0c06490
J. Phys. Chem. C XXXX, XXX, XXX−XXX

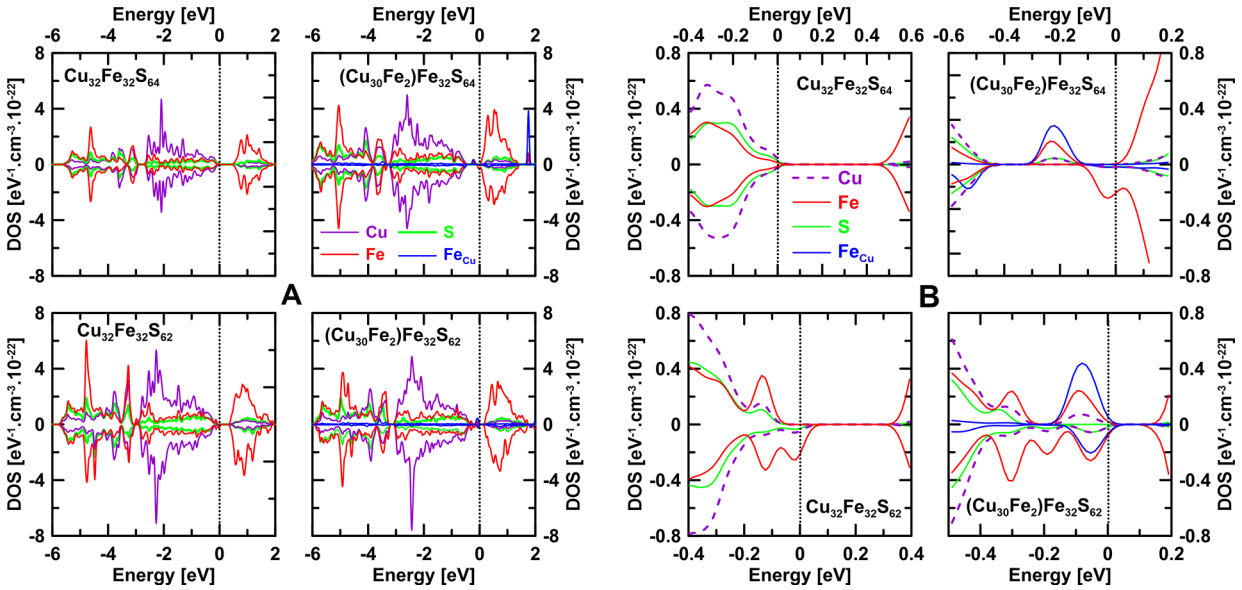

Figure 4. (A) Comparison of the calculated density of states (DOS) projected onto atomic spheres for a formally defect-free structure ($Cu_{32}Fe_{32}S_{64}$) and structures with simulated defects: 6% of Cu sites occupied by Fe ($Cu_{30}Fe_2Fe_{32}S_{64}$), 3% by S vacancies ($Cu_{32}Fe_{32}S_{62}$), and both defects together ($Cu_{30}Fe_2Fe_{32}S_{62}$). (B) The same in detail around the Fermi level.

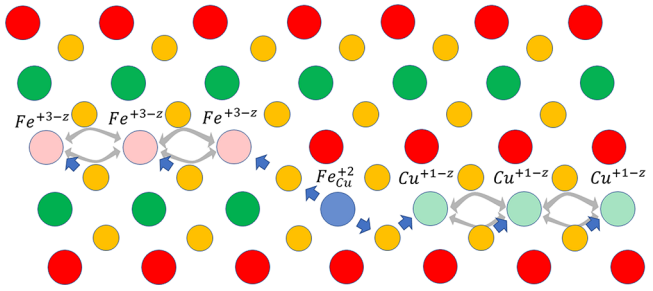

Figure 5. Fe_{Cu} AS defect. This figure depicts two of many plausible (resonant) states that induce a weak FM coupling due to AS defects Fe^{+2}_{Cu}. The blue arrows represent the CT seeded by the AS defect. Left, in the Fe sublattice; right, in the Cu sublattice. z represents the average amplitude of the induced CT. Note that Cu^{+1-z} corresponds to the $3d^{9+z}4s^1$ configuration. Point defects induce mixing of 4s orbitals into the conduction band minimum states. The gray double arrows represent plausible weak sulfur-mediated FM couplings. Red, green, and yellow circles represent iron, copper, and sulfur, respectively. The fading color indicates a change in the oxidation state corresponding to z.

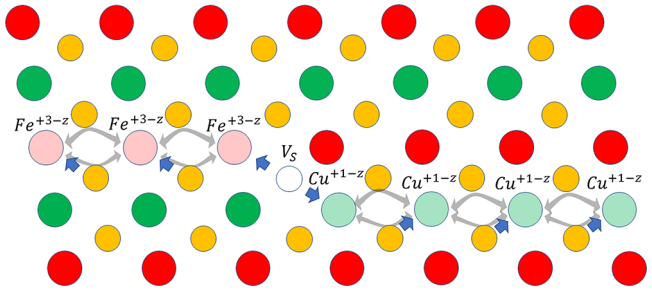

Figure 6. Sulfur vacancy. A sulfur vacancy V_S (blue open circle) can be interpreted as two electrons localized on neighboring Fe/Cu atoms. The defects, thus, formally read as Fe^{+2}−V_S−Fe^{+2}/Cu^0−V_S−Cu^0, which dictates (seeds) the feasible CT along the next neighboring S−Fe/S−Cu bonds (blue arrows) in the horizontal direction (Fe^{+3-z}/Cu^{+1-z} lines). This, in turn, increases the probability of formation of FM chains within CT in the horizontal direction, seeded CTDs. x represents the average amplitude of the induced CT. Note the ordinary CT averages, producing the AFM order otherwise. Sulfur charge is omitted for simplicity. The figure depicts some plausible (resonant) states. Note that each S atom bonds to just two Fe and two Cu atoms, while each Fe (Cu) atom coordinates to four sulfur atoms. The picture is a schematic 2D representation. Red, green, and yellow circles represent iron, copper, and sulfur, respectively. The fading color indicates a decrease in the oxidation state corresponding to z.

weak FM order at elevated temperatures.[33,40] Note that ordinary CT strengthens and retains the AFM exchange within Fe^{+3}−S−Fe^{+3}, although it decreases the magnetic moment of the Fe ions.[4,33,52] In the light of the magnetic measurements discussed below, we anticipate that lone sulfur vacancies occur with a rather low concentration. From this viewpoint, their presence is less obvious in transport and magnetic properties. However, DFT calculations indicated that their combination with iron antisites is more efficient in modifying the band structure and thus the chalcopyrite properties. Specifically, a lone V_S is less efficient in introducing Cu-based states into relevant parts of the band structure. In order to provide a better insight, we present a simple 3D representation of FM induced by Fe_{Cu} point defect in Figure 7. A picture of the FM order induced in Cu sublattice is analogical.

In our view, the defect-induced weak FM coupling facilitates free-carrier transport in $CuFeS_2$ and constitutes a mechanism for the surprisingly high mobility and tiny FM signal observed in AFM $CuFeS_2$ (please see also the discussion of magnetic properties, Seebeck coefficient, and thermal conductivity, which corroborates this conclusion). We understand the seeding as a process of formation of extra band features induced by IPDs. Note that all IPDs or their combination form spin-polarized extra states within the gap (Figure 4A,B). IPDs narrow the band gap due to the formation of extra states in the vicinity of the conduction band minimum or valence band maximum. More importantly, IPDs introduce Cu 3d orbitals into the vicinity of the E_F.

https://dx.doi.org/10.1021/acs.jpcc.0c06490
J. Phys. Chem. C XXXX, XXX, XXX−XXX

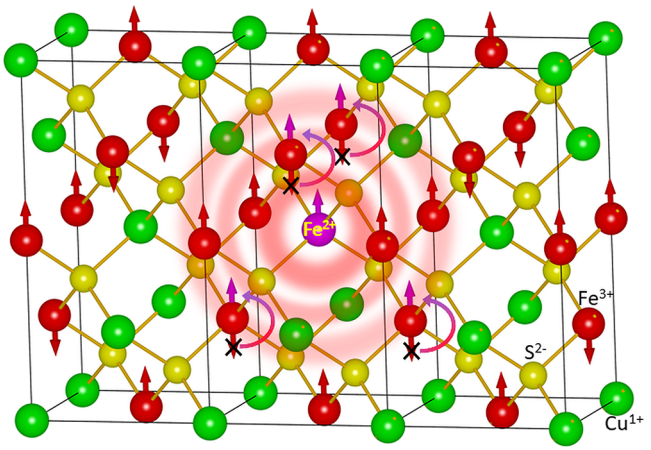

Figure 7. 3D representation of the FM order induced in the Fe sublattice by the AS defect Fe_{Cu} (Fe^{+2}). The FM stems from Fe^{+3}–S^{-2}–Fe^{+2}–S^{-2}–Fe^{+3} (Fe^{+3-z}–S^{-2}–Fe^{+3-z}–S^{-2}–Fe^{+3-z}) bridges.

Thus, with the assistance of DFT calculations, we consider that a combination of two types of free carriers participates in the transport. The first type is connected with FM excitation within $-Fe^{+3}-S^{-2}-Fe^{+2}-S^{-2}-Fe^{+3}-$ bridges; the second type is connected with FM excitations within $-Cu^{+1}-S^{-2}-Cu^{+1}-S^{-2}-Cu^{+1}-$ bridges. The former provides a rather lower mobility of $\mu \approx 10$ cm^2 V^{-1} s^{-1} due to it being a part of the AFM background of Fe. The latter provides a higher mobility of $\mu \approx 100$ cm^2 V^{-1} s^{-1} due to it being formed within the formally diamagnetic (non-polarized) background of Cu. The defect-induced states are detailed in Figure 4A,B. To better visualize the effect of IPDs in the DFT calculations, we assume a much higher concentration of defects (2/32 for FeCu and 2/64 for VS) than that in the real material.

In reality, the presence of defect-induced orbitals within the band gap can be rather low (especially for Cu orbitals) and may span a narrower energy range. Thus, their participation in transport can be strongly dependent on the Fermi level E_F, which may explain the observed free-carrier concentration-dependent mobility (Figure 3). Although DFT calculations are always inaccurate, we argue that they still do reflect the tendency of the system correctly. We note that increasing the number of atoms in the cell 2-fold keeps the DFT outputs comparable. Moreover, a BoltzTrap-derived calculation for both defects shows a negative Seebeck coefficient in contrast to defect free $CuFeS_2$, which is in accordance with the experiment (Supporting Information, section B).

The Fe_{Cu} veraciously reflects the n-type conductivity in terms of Hall and Seebeck coefficient measurements (Figures 2 and 12), which is difficult to obtain for stoichiometric $CuFeS_2$ (Figure 4A,B and Figure 4S). The Fermi level is located at the bottom of the conduction band for the 2/32 concentration. In fact, Fe_{Cu}-derived states merge with the conduction band minimum. We assume that, for lower Fe_{Cu} concentrations, the states remain separated from the minimum, forming a donor level as indicated by experiments.[34,36,39] In contrast, V_S merges the Fermi level into the valence band maximum. This suggests acceptor-like behavior in the low-temperature region (Figure 4S). Notably, both the defects and their combination break the spin-up/spin-down symmetry of the DOS for the strictly AFM order of the hosting structure, implying a local FM order. We note that, in contrast to Fe_{Cu}, the concentration of V_S is generally insensitive to an intentional sulfur stoichiometry variation according to preliminary experiments. We estimate the concentration of Fe_{Cu}^{+2} species involved in FM coupling at 300 K (3 K) as 9×10^{18} (2.3×10^{19}) cm^{-3}, while most of the AS defects ($\approx 10^{20}$ cm^{-3}) form Fe_{Cu}^{+3} resulting in doping. The concentration of V_S is far lower. For details, please see Supporting Information, section D.

3.3. Magnetic Properties. The hysteresis loops evidence a distinct ferromagnetic contribution (Figure 8A,B). We note that Mössbauer spectroscopy corroborates the picture of an AFM matrix with a weak FM contribution (see Supporting Information, section C). The complex and inhomogeneous magnetic state is confirmed from the exchange bias field. Exchange bias is a measure of the interaction between the main AFM phase and minority FM phase. More importantly, the two phases must be magnetically coupled, which corroborates the idea of IPDs induced on the background of an AFM matrix. The field magnitude is proportional to the contact area between the AFM and FM phases. Thus, we observe a coupled mixture of AFM matrix containing FM defects/inclusions. The exchange bias is well observable even for $Cu_{1.02}Fe_{0.98}S_2$ despite its weak hysteresis. (Figure 8A,B); the overstoichiometry of

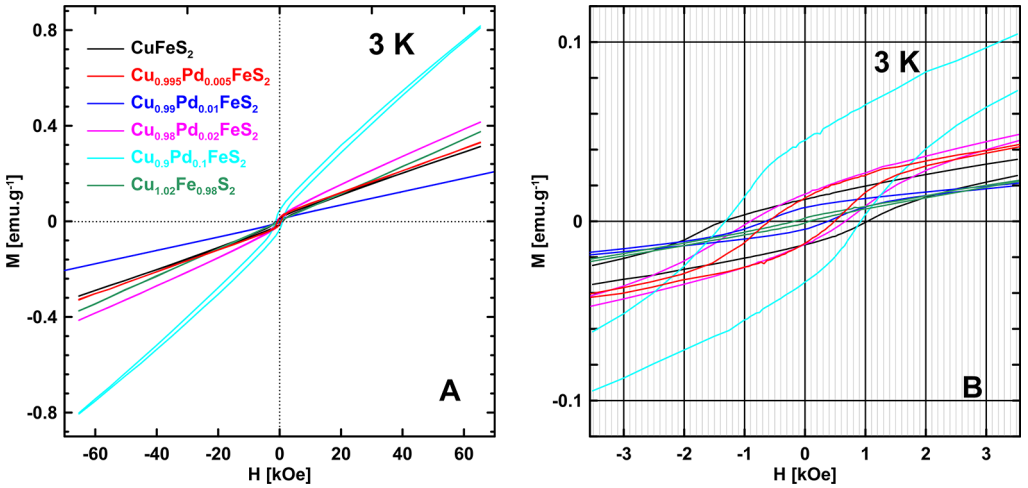

Figure 8. (A, B) Magnetization as a function of magnetic field H for the studied samples at 3 K in the range of (A) $-70 \le H \le 70$ kOe and its magnification (B) $-3.5 \le H \le 3.5$ kOe revealing the observed exchange bias field.

https://dx.doi.org/10.1021/acs.jpcc.0c06490
J. Phys. Chem. C XXXX, XXX, XXX−XXX

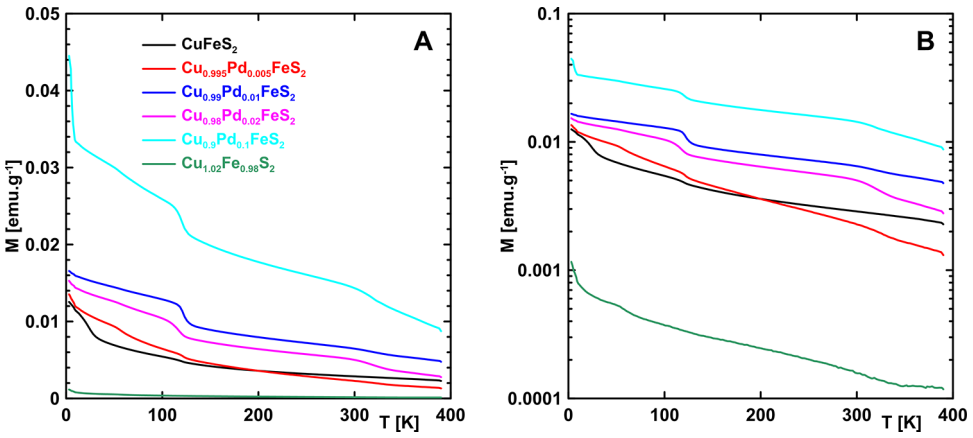

Figure 9. (A, B) Thermoremanence as a function of temperature for $Cu_{1-x}Pd_xFeS_2$ ($0 \geq x \geq 0.1$) and $Cu_{1.02}Fe_{0.98}S_2$ samples on a (A) linear and (B) semi-logarithmic scale. The most pronounced anomaly appears at 120 K (compare with Supporting Information, section D).

copper lowers the concentration of Fe_{Cu} defects resulting in a negligible FM signal and free-carrier concentration (Figure 2). This composition shows the lowest concentration of FM defects, as discussed below. The doped samples show increasing values of coercivity and remanence with increasing Pd concentration. However, both the coercivity and remanence is smaller than that of stoichiometric $CuFeS_2$ for $x < 0.01$, which is consistent with the formation of Pd_{Cu} defects. Similar to the Cu overstoichiometry, a small concentration of Pd led to a decrease in the concentration of Fe_{Cu} and V_S in stoichiometric $CuFeS_2$ (please compare with the discussion of thermoremanence and thermal conductivity). Accordingly, a low concentration of Pd is connected with a low FM signal and vanishing exchange bias. This clearly indicates that the point defects are crucial elements for pinning of the FM phase to the AFM matrix. The observed asymmetry in the remanence (Figure 8B) reveals that not all pinned FM spins are rotated by switching the magnetic field. However, note the exceptional behavior of $CuFeS_2$. This sample shows the highest exchange bias but a vanishing remanence asymmetry, clearly indicating a different nature for the FM. Note that $CuFeS_2$ and $Cu_{0.9}Pd_{0.1}FeS_2$ show a comparable coercivity but different remanence.

To shed more light on this issue, we measured the magnetic thermoremanence (Figure 9A,B). First, upon heating, the doped samples, particularly, and undoped samples, partially, show a well-pronounced decrease in remnant magnetization at ≈120 K. We attribute this behavior to CT defects seeded by Fe_{Cu}, which are coupled to the AFM host structure below the critical temperature of $T_{C1} \approx 120$ K. Another critical temperature appears at $T_{C2} \approx 55$ K for $Cu_{1.02}Fe_{0.98}S_2$. We tentatively attribute this signal to V_S. If true, the Pd substitution for Cu or the shift in Fe/Cu stoichiometry reduces the formation of V_S, as follows from Figures 8 and 9. Clearly, the overstoichiometry of Cu tends to purify the $CuFeS_2$ as for magnetic IPDs. This is consistent with the analysis of thermal conductivity in Section 3.4. However, we observe a $T_{C3} \approx 30$ K for undoped sample $CuFeS_2$ that is difficult to address. After all considerations, we tentatively attribute this FM signal to clustering of Fe_{Cu} and V_S, similar to that observed in $CuInSe_2$.[53] Admittedly, this issue is still open. The fast decrease in the magnetization upon heating due to the paramagnetic background at the lowest temperature is highly pronounced for $Cu_{0.9}Pd_{0.1}FeS_2$ due to a higher free-carrier concentration and PdS. The seeded CT defects can be viewed as a transient state between the $CuFeS_2$ and some derived structures, e.g., FM cubanite $CuFe_2S_3$, which is a well-known process for, e.g., $CuInSe_2$.[53] In contrast to polycrystals, we do observe intergrown cubanite in single-crystalline $CuFeS_2$.

3.4. Thermal Conductivity. Figure 10 depicts the low-temperature thermal conductivity κ from 3 to 300 K. The

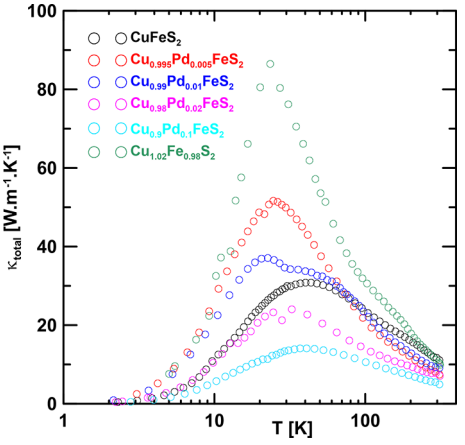

Figure 10. Thermal conductivity as a function of temperature (2−310 K) of $Cu_{1-x}Pd_xFeS_2$ ($0 \geq x \geq 0.1$) and $Cu_{1.02}Fe_{0.98}S_2$ samples.

electronic part of the total thermal conductivity estimated using the Wiedemann−Franz law is negligible (less than 1%) for all samples near room temperature except for the degenerate $Cu_{0.9}Pd_{0.1}FeS_2$ sample (approximately 2%). We notice that the highest peak values for κ are found for the $Cu_{1.02}Fe_{0.98}S_2$ sample (86 W m^{-1} K^{-1} at 23 K), which is consistent with the very low concentration of V_S. Close inspection of the $\kappa = f(T)$ curves reveals the presence of another contribution to the thermal conductivity besides the phononic (and electronic) contribution. This contribution is most pronounced for the $Cu_{0.99}Pd_{0.01}FeS_2$ sample (dark blue circles in Figure 10), appearing as a shoulder on the $\kappa = f(T)$ curve at approximately 30 K. We observe a related effect in the Seebeck coefficient (Section 3.5). We attribute the extra thermal conductivity to magnon-assisted heat transport.[14,54] To estimate the magnitude of this contribution, we assume that, up to approximately 30 K, a phononic contribution dominates, which enables us to fit the $\kappa = f(T)$ dependence of

https://dx.doi.org/10.1021/acs.jpcc.0c06490
J. Phys. Chem. C XXXX, XXX, XXX−XXX

the $Cu_{0.99}Pd_{0.01}FeS_2$ sample up to this temperature using the Debye formula for the phonon thermal conductivity:

$$\kappa_{ph} = \frac{k_B}{2\pi^2 \upsilon}\left(\frac{k_B}{\hbar}\right)^3 T^3 \int_0^{\Theta_D/T} \tau(\omega, T)\frac{x^4 e^x}{(e^x - 1)^2}dx \quad (1)$$

where $\tau(\omega,T)$ is the mean lifetime of a phonon, ω is its angular frequency, υ is the average sound velocity, Θ_D is the Debye temperature (Θ_D = 263 K[55]), and $x = \hbar\omega/k_BT$. τ can be approximated by

$$\tau^{-1} = \frac{\upsilon}{d} + A\omega^4 + B\omega^2 T \exp\left(-\frac{\Theta_D}{CT}\right) \quad (2)$$

where d is the smallest crystal dimension and A, B, and C are fitting parameters independent of temperature. The three terms correspond to phonon scattering at crystal boundaries and point defects and phonon−phonon U processes, respectively. The obtained fit was then extrapolated toward higher temperatures, and the assumed magnetic contribution was calculated by subtracting the phonon part from the experimental part, i.e., $\kappa_{mag} = \kappa_{exp} - \kappa_{ph}$. The estimated error deviations from κ_{ph} are shown by the thick red line in Figure 11. One can see that the magnetic contribution even exceeds

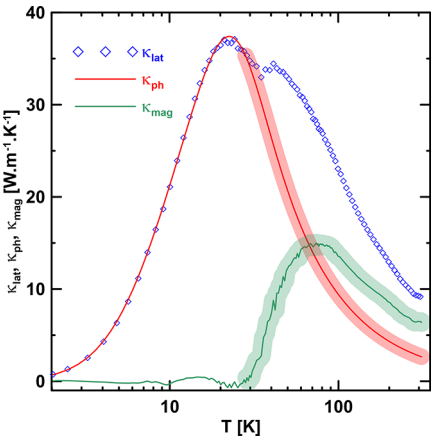

Figure 11. Separation of lattice thermal conductivity (diamonds) into phonon (red line) and magnon (green line) contributions for the $Cu_{0.99}Pd_{0.01}FeS_2$ sample.

the phononic contribution at higher temperatures. Similar contributions are also inherent to other samples, although they are less pronounced in $\kappa \approx f(T)$. Although with an increasing uncertainty, the same procedure indicates that magnons play a non-negligible role in other samples. This is in accordance with the discussion in the sections above and, most importantly, corroborates the fact that the magnon excitation spectrum has a gap of ca. 1.3 THz, which limits the magnon role at low temperatures.[4]

We return now to the analysis of the phonon part of the thermal conductivity. As a starting point, we choose a very small value of A for $Cu_{1.02}Fe_{0.98}S_2$, which indicates an almost defect-free structure (Table 1). The increase in the A parameter indicates the increasing concentration of Pd_{Cu} and Fe_{Cu} due to Pd doping. In addition, we observe a small drop in A for x = 0.005, suggesting that the true substitution of Pd for Cu rather hinders the formation of AS defects, which is in accordance with the comparatively lower magnetization of the slightly doped samples. A further increase in A corresponds to the formation of AS defects due to the shift in the Cu/Fe stoichiometry. The crystalline size L culminates for small x, indicating that substitutional Pd facilitates the growth/quality of microcrystals. The same applies for the overstoichiometry of Cu, although it is not so pronounced. This phenomenon occurs due to eutectic formation.[56] A high content of Pd reduces L profoundly, which is connected with the extensive formation of the extraneous PdS phase. The Umklapp scattering parameter B is difficult to address since it is largely affected by the magnetic contribution κ_{mag}.

3.5. Seebeck Coefficient. Figure 12 summarizes the Seebeck coefficient S as a function of temperature. Negative

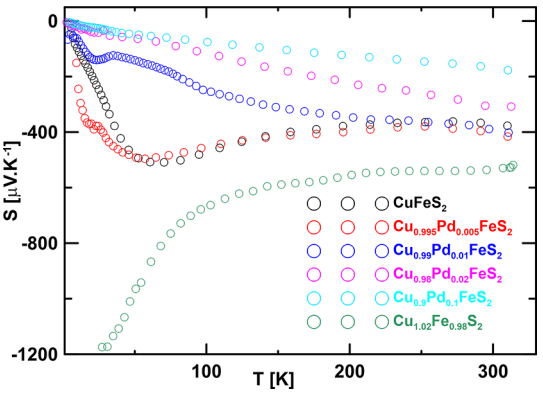

Figure 12. Seebeck coefficient as a function of temperature (2−310 K) for $Cu_{1-x}Pd_xFeS_2$ ($0 \geq x \geq 0.1$) and $Cu_{1.02}Fe_{0.98}S_2$ samples. The $Cu_{1.02}Fe_{0.98}S_2$ sample was measured down to only 30 K due to its high resistivity.

values over the whole temperature range indicate dominant electron transport. However, two of the non-degenerate samples, $CuFeS_2$ and $Cu_{0.995}Pd_{0.005}FeS_2$, show positive values for the Seebeck coefficient at very low temperatures (not shown here), which hint at p-type conductivity; unfortunately, the resistivity of these samples is so high (see Figure 1) that

Table 1. Values of Selected Parameters Obtained by Fitting Experimental Lattice Thermal Conductivities κ_{lat} by Means of Debye Formula (eqs 1 and 2)[a]

sample	A (10^{-43} s^3)	B (10^{-18} s·K^{-1})	L (μm)	ρ/ρ_{cryst} × 100 (%)
$Cu_{1.02}Fe_{0.98}S_2$	0.9 ± 0.3	9.5 ± 1.5	9.0 ± 0.5	98.5
$CuFeS_2$	8.8 ± 0.6	5.5 ± 1.5	5.7 ± 0.3	98.5
$Cu_{0.995}Pd_{0.005}FeS_2$	6.7 ± 0.7	8.0 ± 3.0	20.0 ± 1.0	98.0
$Cu_{0.99}Pd_{0.01}FeS_2$	10.0 ± 1.0	12.0 ± 3.0	18.0 ± 1.0	98.0
$Cu_{0.9}Pd_{0.1}FeS_2$	27. ± 0.5	20.0 ± 1.0	3.7 ± 0.1	~97[b]

[a]Densities of the hot-pressed pellets used for the measurements as compared to theoretical values are listed in the last column. [b]Theoretical value of composite 93.5% wt % of $CuFeS_2$ and 6.5 wt % of PdS was considered for the calculation.[39]

https://dx.doi.org/10.1021/acs.jpcc.0c06490
J. Phys. Chem. C XXXX, XXX, XXX−XXX

the data may be disputable. Similarly, the high resistivity of $Cu_{1.02}Fe_{0.98}S_2$ prevents measurement of the Seebeck coefficient below 30 K. The S values for the samples with high free-carrier concentrations monotonically decrease with temperature, showing a typical behavior for a degenerate semiconductor. However, for non-degenerate samples, the absolute values for S saturate between 200 and 300 K and then drop to zero with decreasing temperature with a peak of approximately 30−50 K in between. This feature has been recently explained by an energy-dependent scattering time due to a hopping mechanism.[34] The energy-dependent scattering can account for the shape of the $S = f(T)$ curves but fails to account for the high mobility. Hence, we suggest an alternative model. In fact, the analysis below shows that an energy-dependent effective mass[34] can account for the temperature dependence of the Seebeck coefficient and the energy-dependent scattering time.

We used the Hall free-carrier concentration n_H to fit the general shape of $S = f(T)$. We excluded the negligible magnitude of the phonon drag component in the studied polycrystalline materials and assumed that the Seebeck coefficient arises mostly due to carrier diffusion. For the pristine sample, we supposed that two types of carriers (electrons) participate in the transport. The first carrier dominates at low temperatures (ca. up to 50 K) and its concentration is constant (see Figure 2), while the other carrier dominates above 50 K and its concentration steeply increases, which is consistent with the Hall measurements (Figure 2). Thus, we assume that we can calculate the diffusive part of the Seebeck coefficient S_d separately in each of the two temperature regions considering that two different types of free carriers govern the electronic transport in the respective regions. We used a simplified model derived by Herrings,[57,58] for moderately doped silicon where S_d is given by

$$S_d = -\frac{k_B}{e}\left[\ln\left(\frac{n}{n_0}\right) + \frac{\Delta\varepsilon}{k_B T}\right] \quad (3)$$

where $\Delta\varepsilon \cong 2k_BT$ is the energy of the electrons relative to the edge of the conduction band, k_B is the Boltzmann constant, and e is the electron charge. n_0 denotes the effective density of states in the conduction band:

$$n_0 = 2\left(\frac{2\pi m_d k_B T}{h^2}\right)^{3/2} \quad (4)$$

where m_d is the density of states effective mass and h is the Planck constant.

Using an effective mass of $m_d = 2.2m_0$ for the carriers dominating at higher temperatures (80−300 K) for the pristine sample,[39] we obtained a reasonable coincidence with the experimental data (empty black circles vs black solid line in Figure 13). To qualitatively describe the further decrease in S with decreasing temperature, we had to use a smaller m_d value. We obtained a best fit for $m_d = 0.7m_0$ in the temperature range of 10−60 K (full black circles vs black solid line in Figure 13). In terms of the point defect picture, we suggest that the lighter electrons are derived mostly from the p states of sulfur and d states of Cu; the heavier electrons share the d states of Fe. This simplified model works well also for the lightly Pd-doped samples ($Cu_{1-x}Pd_xFeS_2$ (x = 0.005, 0.01, 0.02). A comparison of the experimental data and the calculated S_d for the $Cu_{0.99}Pd_{0.01}FeS_2$ sample is also presented in Figure 13 (blue solid line vs empty blue circles). We note that a similar model

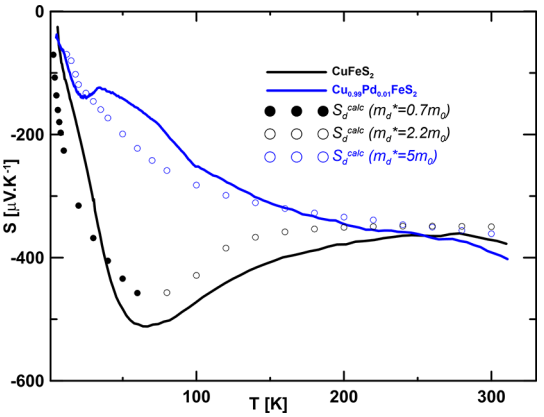

Figure 13. Seebeck coefficient as a function of temperature for $CuFeS_2$ and $Cu_{0.99}Pd_{0.01}FeS_2$ samples. Full lines represent interpolated experimental courses. Symbols represent calculated values.

is inapplicable for the $Cu_{0.9}Pd_{0.1}FeS_2$ sample due to the strong degeneration. Although the diffusive component S_d dominates the total Seebeck coefficient in the samples with lower free-carrier concentrations, one observes another distinct contribution to the S values appearing at low temperatures between 20 and 30 K in the form of a shoulder in the $S = f(T)$ dependence (see Figure 12) for the $Cu_{1-x}Pd_xFeS_2$ samples (x = 0, 0.005, 0.01). Excluding a phonon drag contribution, we attribute this shoulder to a magnetic order-derived contribution (please compare with the discussion for the thermal and magnetic properties).

4. CONCLUSIONS

In the present paper, we attempted to shed more light on the "mysterious" properties of the antiferromagnetic semiconductor $CuFeS_2$. Based on extensive experimental and DFT results, we can summarize the conclusions into the following points:

1. Strictly stoichiometric $CuFeS_2$ shows a clear Fe-generated AFM order and an accordingly low electrical conductivity. However, the strict stoichiometry in the solid state can be achieved only through preparation from the melt with a slight overstoichiometry of Cu (e.g., $Cu_{1.01}Fe_{0.99}S_2$), which relates to a low concentration of intrinsic point defects (IPDs).
2. $CuFeS_2$ prepared from an exactly stoichiometric melt tends to form IPDs, which is connected with the appearance of FM and non-negligible electrical conductivity. The most distinctive IPD is the antisite (AS) defect, with Fe residing in the place of Cu, Fe_{Cu}, which behaves as a donor. Furthermore, sulfur vacancies, V_S, can play a role in influencing the $CuFeS_2$ properties. The IPD concentration can be varied either by changing the stoichiometry (e.g., Cu/Fe) or by extrinsic doping, as in the present case.
3. We can distinguish between two types of FM in otherwise AFM $CuFeS_2$ using exchange bias. The first type is derived from IPD-induced FM defects coupled to the AFM background of the matrix; the second is based on an uncoupled FM due to the presence of extraneous phases.
4. Although the exchange bias is usually connected with the pinning of uncompensated spins on an AFM domain surface, the high mobility suggests that IPD-based

https://dx.doi.org/10.1021/acs.jpcc.0c06490
J. Phys. Chem. C XXXX, XXX, XXX−XXX

exchange bias can also stem from the domain volume in $CuFeS_2$ (compare with ref 47.

5. The comparatively high mobility of electrons in the AFM structure is connected with Cu d orbital/S p orbital-generated states in the vicinity of the Fermi level. These defect-generated states provide a narrow window for mobile electrons. The charge transport is also connected to a weak FM signal in the undoped $CuFeS_2$.
6. We suggest that Fe_{Cu}, V_S, and their combination can seed an FM order within charge transfer (CT) fluctuations that are otherwise AFM in nature. The critical temperatures for the FM order are determined to be $T_{C1} \approx 120$ K, $T_{C2} \approx 55$ K, and $T_{C3} \approx 30$ K. Next to IPD-induced Cu d orbital/S p orbital-generated states, the Fe d orbital-generated states enhance the mobility of electrons. The concentration of a lone V_S is markedly lower than the concentration of Fe_{Cu}. The above conclusions are corroborated also by observation of magnetic contributions in the temperature-dependent thermal conductivity and Seebeck coefficient of samples.
7. The results indicate that intrinsic defect can significantly modify the properties of charge transfer compounds. The modification consists in the seeding of charge transfer nature by point defects.

■ ASSOCIATED CONTENT

Supporting Information

The Supporting Information is available free of charge at https://pubs.acs.org/doi/10.1021/acs.jpcc.0c06490.

A detailed analysis of electrical resistivities (section A), BoltzTrap calculation of Seebeck coefficient (section B), Mössbauer spectroscopy analysis (section C), and magnetic properties above room temperature (section D) (PDF)

■ AUTHOR INFORMATION

Corresponding Author

Čestmír Drašar − *Faculty of Chemical Technology, University of Pardubice, Pardubice 532 10, Czech Republic;* orcid.org/0000-0002-5645-5683; Email: cestmir.drasar@upce.cz

Authors

Jiřá Navrátil − *Faculty of Chemical Technology, University of Pardubice, Pardubice 532 10, Czech Republic; Institute of Physics, Czech Academy of Sciences, Prague 8 182 21, Czech Republic;* orcid.org/0000-0002-8697-9912

Petr Levinský − *Institute of Physics, Czech Academy of Sciences, Prague 8 182 21, Czech Republic*

Jiří Hejtmánek − *Institute of Physics, Czech Academy of Sciences, Prague 8 182 21, Czech Republic*

Mariia Pashchenko − *Institute of Physics, Czech Academy of Sciences, Prague 8 182 21, Czech Republic*

Karel Knížek − *Institute of Physics, Czech Academy of Sciences, Prague 8 182 21, Czech Republic*

Lenka Kubíčková − *Institute of Physics, Czech Academy of Sciences, Prague 8 182 21, Czech Republic;* orcid.org/0000-0001-8928-764X

Tomáš Kmječ − *Faculty of Mathematics and Physics, Charles University, Praha 8 180 00, Czech Republic*

Complete contact information is available at: https://pubs.acs.org/10.1021/acs.jpcc.0c06490

Notes

The authors declare no competing financial interest.

■ ACKNOWLEDGMENTS

Financial support from the Czech Science Foundation (project 18-12761S) was greatly appreciated. The work was further supported by Operational Programme Research, Development and Education financed by European Structural and Investment Funds and the Czech Ministry of Education, Youth and Sports (project SOLID21 - CZ.02.1.01/0.0/0.0/16_019/0000760). L.K. and T.K. would like to acknowledge the financial support under the SVV-2017-260442 project. Further, L.K. would like to thank Dr. Jaroslav Kohout for valuable discussions on the analysis of the Mössbauer spectra.

■ ABBREVIATIONS

AFM; antiferromagnetic; AS; antisite; CT; charge transfer; DFT; density functional theory; DOS; density of states; IPD; intrinsic point defect; FM; ferromagnetic; VRH; variable-range hopping

■ REFERENCES

(1) Goodman, C. H. L.; Douglas, R. W. New semiconducting compounds of diamond type structure. *Physica* **1954**, *20*, 1107−1109.

(2) Austin, I. G.; Goodman, C. H. L.; Pengelly, A. E. Semiconductors with Chalcopyrite Structure. *Nature* **1956**, *178*, 433.

(3) Austin, I. G.; Goodman, C. H. L.; Pengelly, A. E. New Semiconductors with the Chalcopyrite Structure. *J. Electrochem. Soc.* **1956**, *103*, 609−610.

(4) Donnay, G.; Corliss, L. M.; Donnay, J. D. H.; Elliott, N.; Hastings, J. M. Symmetry of magnetic structures: Magnetic structure of chalcopyrite. *Phys. Rev.* **1958**, *112*, 1917−1923.

(5) Teranishi, T. Magnetic and Electric Properties of Chalcopyrite. *J. Phys. Soc. Jpn.* **1961**, *16*, 1881−1887.

(6) Teranishi, T.; Sato, K. Optical, Electrical and Magnetic Properties of Chalcopyrite, $CuFeS_2$. *J. Phys. Colloq.* **1975**, *36*, 149−153.

(7) Oguchi, T.; Sato, K.; Teranishi, T. Optical Reflectivity Spectrum of a $CuFeS_2$ Single Crystal. *J. Phys. Soc. Jpn.* **1980**, *48*, 123−128.

(8) Tossell, J. A.; Urch, D. S.; Vaughan, D. J.; Wiech, G. The electronic structure of $CuFeS_2$, chalcopyrite, from x-ray emission and x-ray photoelectron spectroscopy and X-alpha calculations. *J. Chem. Phys.* **1982**, *77*, 77−82.

(9) Robie, R. A.; Wiggins, L. B.; Barton, P. B., Jr.; Hemingway, B. S. Low-temperature heat capacity and entropy of chalcopyrite ($CuFeS_2$): estimates of the standard molar enthalpy and Gibbs free energy of formation of chalcopyrite and bornite (Cu_5FeS_4). *J. Chem. Thermodyn.* **1985**, *17*, 481−488.

(10) Wu, Y.; Zhou, B.; Yang, C.; Liao, S.; Zhang, W. H.; Li, C. $CuFeS_2$ colloidal nanocrystals as an efficient electrocatalyst for dye sensitized solar cells. *Chem. Commun.* **2016**, *52*, 11488−11491.

(11) Baltz, V.; Manchon, A.; Tsoi, M.; Moriyama, T.; Ono, T.; Tserkovnyak, Y. Antiferromagnetic spintronics. *Rev. Mod. Phys.* **2018**, *90*, 15005.

(12) Tsujii, N.; Mori, T. High Thermoelectric Power Factor in a Carrier-Doped Magnetic Semiconductor $CuFeS_2$. *Appl. Phys. Express* **2013**, *6*, 043001−043004.

(13) Tsujii, N.; Mori, T.; Isoda, Y. Phase stability and thermoelectric properties of $CuFeS_2$-based magnetic semiconductor. *J. Electron. Mater.* **2014**, *43*, 2371−2375.

(14) Ang, R.; Khan, A. U.; Tsujii, N.; Takai, K.; Nakamura, R.; Mori, T. Thermoelectricity Generation and Electron-Magnon Scattering in a Natural Chalcopyrite Mineral from a Deep-Sea Hydrothermal Vent. *Angew. Chem., Int. Ed.* **2015**, *54*, 12909−12913.

(15) Lefévre, R.; et al. Thermoelectric properties of the chalcopyrite $Cu_{1-x}M_xFeS_{2-y}$ series (M = Mn, Co, Ni). *RSC Adv.* **2016**, *6*, 55117−55124.
(16) Takaki, H.; et al. Thermoelectric properties of a magnetic semiconductor $CuFeS_2$. *Mater. Today Phys.* **2017**, *3*, 85−92.
(17) Pauling, L.; Brockway, L. O. The Crystal Structure of Chalcopyrite $CuFeS_2$. *J. Crystallogr. Cryst. Mater.* **1932**, *82*, 188.
(18) Zaanen, J.; Sawatzky, G. A. The electronic structure and superexchange interactions in transition-metal compounds. *Can. J. Phys.* **1987**, *65*, 1262−1271.
(19) Fujisawa, M.; Suga, S.; Mizokawa, T.; Fujimori, A.; Sato, K. Electronic structures of $CuFeS_2$ and $CuAl_{0.9}Fe_{0.1}S_2$ studied by electron and optical spectroscopies. *Phys. Rev. B* **1994**, *49*, 7155−7164.
(20) Burdick, C. L.; Ellis, J. H. The Crystal Structure of Chalcopyrite Determined by X Rays. *J. Am. Chem. Soc.* **Dec. 1917**, *39*, 2518−2525.
(21) MacLean, W. H.; Cabri, L. J.; Gill, J. E. Exsolution Products in Heated Chalcopyrite. *Can. J. Earth Sci.* **1972**, *9*, 1305−1317.
(22) Woolley, J. C.; Lamarche, A.-M.; Lamarche, G.; Brun Del Re, R.; Quintero, M.; Swainson, I. P.; Holden, T. M. Low temperature magnetic behaviour of $CuFeS_2$ from neutron diffraction data. *J. Magn. Magn. Mater.* **1996**, *164*, 154−162.
(23) Sato, K.; Harada, Y.; Taguchi, M.; Shin, S.; Fujimori, A. Characterization of Fe 3d states in $CuFeS_2$ by resonant X-ray emission spectroscopy. *Phys. Status Solidi Appl. Mater. Sci.* **2009**, *206*, 1096−1100.
(24) Boekema, C.; et al. Cu and Fe valence states in $CuFeS_2$. *J. Magn. Magn. Mater.* **2004**, *272-276*, 559−561.
(25) Kambara, T. Optical Properties of a Magnetic Semiconductor: Chalcopyrite CuFeS. II. Calculated Electronic Structures of CuGaS2:Fe and CuFeS2. *J. Phys. Soc. Jpn.* **Jun. 1974**, *36*, 1625−1635.
(26) Hamajima, T.; Kambara, T.; Gondaira, K. I.; Oguchi, T. Self-consistent electronic structures of magnetic semiconductors by a discrete variational Xα calculation. III. Chalcopyrite $CuFeS_2$. *Phys. Rev. B* **1981**, *24*, 3349−3353.
(27) Goh, S. W.; Buckley, A. N.; Lamb, R. N.; Rosenberg, R. A.; Moran, D. The oxidation states of copper and iron in mineral sulfides, and the oxides formed on initial exposure of chalcopyrite and bornite to air. *Geochim. Cosmochim. Acta* **2006**, *70*, 2210−2228.
(28) Klekovkina, V. V.; Gainov, R. R.; Vagizov, F. G.; Dooglav, A. V.; Golovanevskiy, V. A.; Pen'kov, I. N. Oxidation and magnetic states of chalcopyrite $CuFeS_2$: A first principles calculation. *Opt. Spectrosc.* **2014**, *116*, 885−888.
(29) Knight, K. S.; Marshall, W. G.; Zochowski, S. W. The low-temperature and high-pressure thermoelastic and structural properties of chalcopyrite, CuFeS2. *Can. Mineral.* **2011**, *49*, 1015−1034.
(30) Lovesey, S. W.; Knight, K. S.; Detlefs, C.; Huang, S. W.; Scagnoli, V.; Staub, U. Acentric magnetic and optical properties of chalcopyrite (CuFeS2). *J. Phys.: Condens. Matter* **2012**, *24*, 216001.
(31) Pearce, C. I.; Pattrick, R. A. D.; Vaughan, D. J. Electrical and magnetic properties of sulfides. *Rev. Mineral. Geochem.* **2006**, *61*, 127−180.
(32) Khaledialidusti, R.; Mishra, A. K.; Barnoush, A. Temperature-dependent properties of magnetic $CuFeS_2$ from first-principles calculations: Structure, mechanics, and thermodynamics. *AIP Adv.* **2019**, *9*, 065021.
(33) Conejeros, S.; Alemany, P.; Llunell, M.; Moreira, I. D. P. R.; Sánchez, V.; Llanos, J. Electronic Structure and Magnetic Properties of $CuFeS_2$. *Inorg. Chem.* **2015**, *54*, 4840−4849.
(34) Xie, H.; et al. Anomalously Large Seebeck Coefficient of $CuFeS_2$ Derives from Large Asymmetry in the Energy Dependence of Carrier Relaxation Time. *Chem. Mater.* **2020**, *32*, 2639−2646.
(35) Li, J.; Tan, Q.; Li, J. F. Synthesis and property evaluation of CuFeS2-x as earth-abundant and environmentally-friendly thermoelectric materials. *J. Alloys Compd.* **2013**, *551*, 143−149.
(36) Li, Y.; et al. Thermoelectric transport properties of diamond-like $Cu_{1-x}Fe_{1+x}S_2$ tetrahedral compounds. *J. Appl. Phys.* **2014**, *116*, 203705.
(37) Xie, H.; et al. The Role of Zn in Chalcopyrite $CuFeS_2$: Enhanced Thermoelectric Properties of $Cu_{1-x}Zn_xFeS_2$ with In Situ Nanoprecipitates. *Adv. Energy Mater.* **2017**, *7*, 1−14.
(38) Xie, H.; et al. Thermoelectric performance of $CuFeS_{2+2x}$ composites prepared by rapid thermal explosion. *NPG Asia Mater.* **2017**, *9*, e390.
(39) Navratil, J.; et al. Thermoelectric and Transport Properties of n-type Palladium-Doped Chalcopyrite Cu(1-x)Pd(x)FeS(2) Compounds. *J. Electron. Mater.* **2019**, *48*, 1795−1804. PXRD analysis of the $Cu_{1-x}Pd_xFeS_2$ samples revealed a rather low solubility limit of Pd atoms in the system ($x \approx 0.013$). Formation of extraneous PdS was observed above this limit, which shifts the system to Cu-poor, Fe-rich composition. Corresponding transfer of Fe to Cu sublattice leads to formation of native point defect Fe_{Cu}^{2+}.
(40) Engin, T. E.; Powell, A. V.; Hull, S. A high temperature diffraction-resistance study of chalcopyrite, CuFeS2. *J. Solid State Chem.* **2011**, *184*, 2272−2277.
(41) Žák, T.; Jirásková, Y. CONFIT: Mossbauer spectra fitting program. *Surf. Interface Anal.* **2006**, *38*, 710−714.
(42) Lagarec, K.; Rancourt, D. G. *Recoil - Mössbauer spectral analysis software for Windows;* Canada: University of Ottawa, 1998.
(43) Blaha, P.; Schwarz, K.; Tran, F.; Laskowski, R.; Madsen, G. K. H.; Marks, L. D. WIEN2k: An APW+lo program for calculating the properties of solids. *J. Chem. Phys.* **2020**, *152*, 7.
(44) Perdew, J. P.; Burke, K.; Ernzerhof, M. Generalized gradient approximation made simple. *Phys. Rev. Lett.* **1996**, *77*, 3865−3868.
(45) Madsen, G. K. H.; Singh, D. J. BoltzTraP. A code for calculating band-structure dependent quantities. *Comput. Phys. Commun.* **2006**, *175*, 67−71.
(46) Li, B.; Huang, L.; Zhong, M.; Wei, Z.; Li, J. Electrical and magnetic properties of FeS_2 and $CuFeS_2$ nanoplates. *RSC Adv.* **2015**, *5*, 91103−91107.
(47) Mott, N.; Davis, E. *Electronic Prosses In Non-Crystalline Material;* Oxford, U.K.: Clarendon Press, 1971.
(48) Avdonin, A.; Skupiński, P.; Grasza, K. Hall effect in hopping regime. *Phys. B* **2016**, *483*, 13−18.
(49) Zhou, M.; Gao, X.; Cheng, Y.; Chen, X.; Cai, L. Structural, electronic, and elastic properties of $CuFeS_2$: first-principles study. *Appl. Phys. A: Mater. Sci. Process.* **2014**, *118*, 1145−1152.
(50) Goodenough, J. B. Theory of the role of covalence in the perovskite-type manganites [La,M(II)]MnO_3. *Phys. Rev.* **1955**, *100*, 564−573.
(51) Kanamori, J. Superexchange interaction and symmetry properties of electron orbitals. *J. Phys. Chem. Solids* **1959**, *10*, 87−98.
(52) *. We note that the surface of crystals tends to lose sulfur. In that sense, the surface is seeding area for FM ordering par excellence and can be a center of FM and high mobility.
(53) Zhang, S. B.; Wei, S. H.; Zunger, A.; Katayama-Yoshida, H. Defect physics of the CuInSe2 chalcopyrite semiconductor. *Phys. Rev. B* **1998**, *57*, 9642−9656.
(54) Harris, M. J.; Zinkin, M. P.; Swainson, I. P. Phonons and spin waves in the magnetic semiconductor chalcopyrite. *Phys. Rev. B* **1997**, *55*, 6957−6959.
(55) Ok, H. N.; Baek, K. S.; Choi, E. J. Mössbauer Study of Antiferromagnetic $CuFeS_{2-x}Se_x$. *Phys. Rev. B* **1994**, *50*, 10327−10330.
(56) Čermák, P.; et al. Thermoelectric properties and stability of Tl-doped SnS. *J. Alloys Compd.* **2019**, *811*, 151902.
(57) Herring, C. Theory of the thermoelectric power of semiconductors. *Phys. Rev.* **1954**, *96*, 1163−1187.
(58) Weber, L.; Gmelin, E. Transport properties of silicon. *Appl. Phys. A Solids Surfaces* **1991**, *53*, 136−140.

https://dx.doi.org/10.1021/acs.jpcc.0c06490
J. Phys. Chem. C XXXX, XXX, XXX−XXX